Microscopic self-consistent description of induced fission dynamics: Finite-temperature effects

Zhao, Jie; Nikšić, Tamara; Vretenar, Dario; Zhou, Shan-Gui

Microscopic self-consistent description of induced fission dynamics: Finite-temperature effects

Jie Zhao (赵杰),[1] Tamara Nikšić,[2] Dario Vretenar,[2] and Shan-Gui Zhou (周善贵)[3,4,5,6]

[1]*Microsystem and Terahertz Research Center and Insititute of Electronic Engineering, China Academy of Engineering Physics, Chengdu 610200, Sichuan, China*

[2]*Physics Department, Faculty of Science, University of Zagreb, Bijenička Cesta 32, Zagreb 10000, Croatia*

[3]*CAS Key Laboratory of Theoretical Physics, Institute of Theoretical Physics, Chinese Academy of Sciences, Beijing 100190, China*

[4]*School of Physical Sciences, University of Chinese Academy of Sciences, Beijing 100049, China*

[5]*Center of Theoretical Nuclear Physics, National Laboratory of Heavy Ion Accelerator, Lanzhou 730000, China*

[6]*Synergetic Innovation Center for Quantum Effects and Application, Hunan Normal University, Changsha 410081, China*

(Received 16 September 2018; published 22 January 2019)

The dynamics of induced fission of ^{226}Th is investigated in a theoretical framework based on the finite-temperature time-dependent generator coordinate method (TDGCM) in the Gaussian overlap approximation (GOA). The thermodynamical collective potential and inertia tensor at temperatures in the interval $T =$ 0–1.25 MeV are calculated using the self-consistent multidimensionally constrained relativistic mean-field (MDC-RMF) model, based on the energy density functional DD-PC1. Pairing correlations are treated in the BCS approximation with a separable pairing force of finite range. Constrained RMF+BCS calculations are carried out in the collective space of axially symmetric quadrupole and octupole deformations for the asymmetric fissioning nucleus ^{226}Th. The collective Hamiltonian is determined by the temperature-dependent free energy surface and perturbative cranking inertia tensor, and the TDGCM+GOA is used to propagate the initial collective state in time. The resulting charge and mass fragment distributions are analyzed as functions of the internal excitation energy. The model can qualitatively reproduce the empirical triple-humped structure of the fission charge and mass distributions already at $T = 0$, but the precise experimental position of the asymmetric peaks and the symmetric-fission yield can only be accurately reproduced when the potential and inertia tensor of the collective Hamiltonian are determined at finite temperature, in this particular case between $T = 0.75$ MeV and $T = 1$ MeV.

DOI: 10.1103/PhysRevC.99.014618

I. INTRODUCTION

Fragment distributions present basic fission observables that can be used to assess and validate theoretical methods [1]. For instance, the experimental study of 70 short-lived radioactive isotopes in the region $85 \leqslant Z \leqslant 92$ has shown that the charge and mass yields are symmetric in the lighter mass region, whereas the yields tend to be asymmetric for heavier nuclei and relatively low excitation energies [2]. The charge and mass distributions remain asymmetric up to Cf [3]. The probability of symmetric fission increases with excitation energy because of the weakening of shell effects [4–12].

A microscopic theoretical approach capable of predicting fission fragment distributions starting from the initial state of the compound nucleus is the time-dependent generator coordinate method (TDGCM) [1,13]. In the Gaussian overlap approximation (GOA) the GCM Hill-Wheeler equation reduces to a local, time-dependent Schrödinger-like equation in the space of collective coordinates. For a choice of collective coordinates, the essential inputs are the potential and inertia tensor that can be determined microscopically in a self-consistent mean-field deformation-constrained calculation. Most applications of the TDGCM+GOA to nuclear fission dynamics have been based on nonrelativistic Skyrme and Gogny functionals [13–21]. More recently, relativistic energy density functionals [22–24] have also been employed in the description of fission properties of heavy and superheavy nuclei [25–38]. Triaxial and octupole deformations [39], and the effect of coupling between shape and pairing degrees of freedom [40] on dynamic spontaneous fission paths and half-lives were analyzed using the multidimensionally constrained relativistic mean-field (MDC-RMF) [35] and the relativistic Hartree Bogoliubov (MDC-RHB) model [41]. The first study of fission dynamics that used the TDGCM+GOA based on a relativistic energy density functional was recently reported in Ref. [42], where the effect of pairing correlations on the charge yields and total kinetic energy of fission fragments was examined.

In all applications of the TDGCM+GOA to studies of induced fission dynamics [14,15,18,20,42], the collective potential and inertia tensor have been calculated at zero temperature. However, as the internal excitation energy increases, one expects that both the potential energy surface (PES) and the mass parameters exhibit significant modifications. Finite-temperature (FT) nuclear density functional theory (DFT) [43] provides a convenient framework in which the evolution of a PES and inertia tensor with excitation energy can be described. Several studies of the dependence of PESs and fission barriers on excitation energy have been carried out using the finite-temperature Hartree-Fock-Bogoliubov

(FT-HFB) method based on nonrelativistic Skyrme [44–48] and Gogny functionals [49]. The effect of FT on perturbative cranking inertia tensors has also been investigated in the FT-HFB framework [44,49]. Exploratory studies of FT effects on induced fission yield distributions using semiclassical approaches have been reported in Refs. [50–52]. In this work we present the first microscopic investigation of finite-temperature effects on induced fission dynamics using the TDGCM+GOA collective model. The theoretical framework and method are introduced in Sec. II. The details of the calculation for the illustrative example of ^{226}Th, the results for deformation energy landscapes, inertia tensor, as well as the charge and mass yield distributions are described and discussed in Sec. III. Sec. IV contains a summary of the principal results.

II. METHOD

Assuming that the compound nucleus is in a state of thermal equilibrium at temperature T, it can be described by the finite-temperature (FT) Hartree-Fock-Bogoliubov (HFB) theory [43,53]. In the grand-canonical ensemble, the expectation value of any operator $\hat{O}$ is given by an ensemble average

$$\langle \hat{O} \rangle = \mathrm{Tr}\,[\hat{D}\hat{O}], \tag{1}$$

where $\hat{D}$ is the density operator:

$$\hat{D} = \frac{1}{Z} e^{-\beta(\hat{H}-\lambda\hat{N})}. \tag{2}$$

Z is the grand partition function, $\beta = 1/k_B T$ with the Boltzmann constant k_B, $\hat{H}$ is the Hamiltonian of the system, λ denotes the chemical potential, and $\hat{N}$ is the particle number operator. In the present study we employ the relativistic mean-field (RMF) model for the particle-hole channel, while pairing correlations are treated in the BCS approximation. The Dirac single-nucleon equation

$$\hat{h}\psi_k(\boldsymbol{r}) = \epsilon_k \psi_k(\boldsymbol{r}), \tag{3}$$

is determined by the Hamiltonian

$$\hat{h} = \boldsymbol{\alpha}\cdot\boldsymbol{p} + \beta[M + S(\boldsymbol{r})] + V_0(\boldsymbol{r}) + \Sigma_R(\boldsymbol{r}), \tag{4}$$

where, for the relativistic energy-density functional DD-PC1 [54], the scalar potential, vector potential, and rearrangement terms read

$$\begin{aligned} S &= \alpha_S(\rho)\rho_S + \delta_S \triangle \rho_S, \\ V_0 &= \alpha_V(\rho)\rho_V + \alpha_{TV}(\rho)\vec{\rho}_{TV}\cdot\vec{\tau} + e\frac{1-\tau_3}{2}A_0, \\ \Sigma_R &= \frac{1}{2}\frac{\partial\alpha_S}{\partial\rho}\rho_S^2 + \frac{1}{2}\frac{\partial\alpha_V}{\partial\rho}\rho_V^2 + \frac{1}{2}\frac{\partial\alpha_{TV}}{\partial\rho}\rho_{TV}^2, \end{aligned} \tag{5}$$

respectively. M is the nucleon mass, $\alpha_S(\rho)$, $\alpha_V(\rho)$, and $\alpha_{TV}(\rho)$ are density-dependent couplings for different space-isospace channels, δ_S is the coupling constant of the derivative term, and e is the electric charge. In the finite-temperature RMF+BCS approximation the single-nucleon densities ρ_S (scalar-isoscalar density), ρ_V (timelike component of the isoscalar current), and ρ_{TV} (timelike component of the isovector current), are defined by the following relations:

$$\rho_S = \sum_k \bar{\psi}_k(\boldsymbol{r})\psi_k(\boldsymbol{r})\big[v_k^2(1-f_k) + u_k^2 f_k\big], \tag{6}$$

$$\rho_V = \sum_k \bar{\psi}_k(\boldsymbol{r})\gamma^0\psi_k(\boldsymbol{r})\big[v_k^2(1-f_k) + u_k^2 f_k\big], \tag{7}$$

$$\rho_{TV} = \sum_k \bar{\psi}_k(\boldsymbol{r})\vec{\tau}\gamma^0\psi_k(\boldsymbol{r})\big[v_k^2(1-f_k) + u_k^2 f_k\big], \tag{8}$$

where f_k is the thermal occupation probability of a quasiparticle state

$$f_k = \frac{1}{1+e^{\beta E_k}}, \tag{9}$$

and $\beta = 1/k_B T$. $E_k = [(\epsilon_k - \lambda)^2 + \Delta_k^2]^{1/2}$ is the quasiparticle energy, and λ is the Fermi level. v_k^2 are the BCS occupation probabilities

$$v_k^2 = \frac{1}{2}\left(1 - \frac{\epsilon_k - \lambda}{E_k}\right), \tag{10}$$

and $u_k^2 = 1 - v_k^2$. The gap equation at finite temperature reads

$$\Delta_k = \frac{1}{2}\sum_{k'>0} V^{pp}_{k\bar{k}k'\bar{k}'}\frac{\Delta_{k'}}{E_{k'}}(1-2f'_k). \tag{11}$$

In the particle-particle channel we use a separable pairing force of finite range [55]:

$$V(\mathbf{r}_1,\mathbf{r}_2,\mathbf{r}'_1,\mathbf{r}'_2) = G_0\,\delta(\mathbf{R}-\mathbf{R}')P(\mathbf{r})P(\mathbf{r}')\tfrac{1}{2}(1-P^\sigma), \tag{12}$$

where $\mathbf{R} = (\mathbf{r}_1 + \mathbf{r}_2)/2$ and $\mathbf{r} = \mathbf{r}_1 - \mathbf{r}_2$ denote the center-of-mass and the relative coordinates, respectively. $P(\mathbf{r})$ reads

$$P(\mathbf{r}) = \frac{1}{(4\pi a^2)^{3/2}} e^{-\mathbf{r}^2/4a^2}. \tag{13}$$

The two parameters of the interaction were originally adjusted to reproduce the density dependence of the pairing gap in nuclear matter at the Fermi surface calculated with the D1S parametrization of the Gogny force [13].

The entropy of the compound nuclear system is computed using the relation:

$$S = -k_B \sum_k [f_k \ln f_k + (1-f_k)\ln(1-f_k)]. \tag{14}$$

The thermodynamical potential relevant for an analysis of finite-temperature deformation effects is the Helmholtz free energy $F = E(T) - TS$, evaluated at constant temperature T [45]. $E(T)$ is the binding energy of the deformed nucleus, and the deformation-dependent energy landscape is obtained in a self-consistent finite-temperature mean-field calculation with constraints on the mass multipole moments $Q_{\lambda\mu} = r^\lambda Y_{\lambda\mu}$. The nuclear shape is parameterized by the deformation parameters

$$\beta_{\lambda\mu} = \frac{4\pi}{3AR^\lambda}\langle Q_{\lambda\mu}\rangle. \tag{15}$$

The shape is assumed to be invariant under the exchange of the x and y axes, and all deformation parameters $\beta_{\lambda\mu}$ with

even μ can be included simultaneously. The self-consistent RMF+BCS equations are solved by an expansion in the axially deformed harmonic oscillator (ADHO) basis [56]. In the present study calculations have been performed in an ADHO basis truncated to $N_f = 20$ oscillator shells. For details of the MDC-RMF model we refer the reader to Ref. [35].

In the TDGCM+GOA nuclear fission is modeled as a slow adiabatic process driven by only a few collective degrees of freedom [18]. The dynamics is described by a local, time-dependent Schrödinger-like equation in the space of collective coordinates $\boldsymbol{q}$,

$$i\hbar\frac{\partial g(\boldsymbol{q},t)}{\partial t} = \hat{H}_{\rm coll}(\boldsymbol{q})g(\boldsymbol{q},t). \tag{16}$$

The Hamiltonian $\hat{H}_{\rm coll}(\boldsymbol{q})$ reads

$$\hat{H}_{\rm coll}(\boldsymbol{q}) = -\frac{\hbar^2}{2}\sum_{ij}\frac{\partial}{\partial q_i}B_{ij}(\boldsymbol{q})\frac{\partial}{\partial q_j} + V(\boldsymbol{q}), \tag{17}$$

where $V(\boldsymbol{q})$ is the collective potential, and the inertia tensor $B_{ij}(\boldsymbol{q}) = \mathcal{M}^{-1}(\boldsymbol{q})$ is the inverse of the mass tensor $\mathcal{M}$. Both the potential and mass tensor are determined by microscopic self-consistent mean-field calculations based on universal energy density functionals. $g(\boldsymbol{q},t)$ is the complex wave function of the collective variables $\boldsymbol{q}$. In the present case the variables $\boldsymbol{q}$ correspond to the quadrupole $\langle Q_{20}\rangle$ and octupole $\langle Q_{30}\rangle$ mass multipole moments.

The collective space is divided into an inner region with a single nuclear density distribution, and an external region that contains the two fission fragments. The set of scission configurations defines the hypersurface that separates the two regions. The flux of the probability current through this hypersurface provides a measure of the probability of observing a given pair of fragments at time t. Each infinitesimal surface element is associated with a given pair of fragments (A_L, A_H), where A_L and A_H denote the lighter and heavier fragments, respectively. The integrated flux $F(\xi,t)$ for a given surface element ξ is defined as [16]

$$F(\xi,t) = \int_{t_0}^{t}\int_{\xi}\boldsymbol{J}(\boldsymbol{q},t)\cdot d\boldsymbol{S}, \tag{18}$$

where $\boldsymbol{J}(\boldsymbol{q},t)$ is the current

$$\boldsymbol{J}(\boldsymbol{q},t) = \frac{\hbar}{2i}\boldsymbol{B}(\boldsymbol{q})[g^*(\boldsymbol{q},t)\nabla g(\boldsymbol{q},t) - g(\boldsymbol{q},t)\nabla g^*(\boldsymbol{q},t)]. \tag{19}$$

The yield for the fission fragment with mass A is defined by

$$Y(A) \propto \sum_{\xi\in\mathcal{A}}\lim_{t\to\infty}F(\xi,t). \tag{20}$$

The set $\mathcal{A}(\xi)$ contains all elements belonging to the scission hypersurface such that one of the fragments has mass number A.

The mass tensor is calculated in the finite-temperature perturbative cranking approximation [44,49]:

$$\mathcal{M}^{Cp} = \hbar^2 M_{(1)}^{-1}M_{(3)}M_{(1)}^{-1}, \tag{21}$$

with

$$[M_{(k)}]_{ij,T} = \frac{1}{2}\sum_{\mu\neq\nu}\langle 0|\hat{Q}_i|\mu\nu\rangle\langle\mu\nu|\hat{Q}_j|0\rangle\left\{\frac{(u_\mu u_\nu - v_\mu v_\nu)^2}{(E_\mu - E_\nu)^k}\left[\tanh\left(\frac{E_\mu}{2k_BT}\right) - \tanh\left(\frac{E_\nu}{2k_BT}\right)\right]\right\}$$
$$+\frac{1}{2}\sum_{\mu\nu}\langle 0|\hat{Q}_i|\mu\nu\rangle\langle\mu\nu|\hat{Q}_j|0\rangle\left\{\frac{(u_\mu v_\nu + u_\nu v_\mu)^2}{(E_\mu + E_\nu)^k}\left[\tanh\left(\frac{E_\mu}{2k_BT}\right) + \tanh\left(\frac{E_\nu}{2k_BT}\right)\right]\right\}. \tag{22}$$

The starting point of the dynamical calculation is the choice of the collective wave packet $g(\boldsymbol{q}, t=0)$. We build the initial state as a Gaussian superposition of the quasibound states g_k,

$$g(\boldsymbol{q}, t=0) = \sum_k \exp\left(\frac{(E_k - \bar{E})^2}{2\sigma^2}\right)g_k(\boldsymbol{q}), \tag{23}$$

where the value of the parameter σ is set to 0.5 MeV. The collective states $\{g_k(\boldsymbol{q})\}$ are solutions of the stationary eigenvalue equation in which the original collective potential $V(\boldsymbol{q})$ is replaced by a new potential $V'(\boldsymbol{q})$ that is obtained by extrapolating the inner potential barrier with a quadratic form (see Ref. [16] for details). In the following we denote the average energy of the collective initial state by $E^*_{\rm coll.}$, and its value will usually be chosen about 1 MeV above the highest fission barrier. The mean energy $\bar{E}$ in Eq. (23) is then adjusted iteratively in such a way that $\langle g(t=0)|\hat{H}_{\rm coll}|g(t=0)\rangle = E^*_{\rm coll.}$. Just as in the study of thermal fission rates with temperature-dependent fission barriers of Ref. [44], the beyond-mean-field corrections to the thermodynamical collective potential have not been included in this work.

III. INDUCED FISSION DYNAMICS OF ^{226}Th: RESULTS AND DISCUSSION

As in our first illustrative application of the TDGCM+GOA framework to a description of induced fission dynamics [42], we consider the case of ^{226}Th and analyze the temperature dependence of fission barriers, perturbative cranking inertia tensors, and distribution of charge and mass yields. In the present study the collective coordinates are the axially symmetric quadrupole deformation parameter β_{20} and octupole deformation parameter β_{30}. The starting point is a large-scale deformation-constrained finite-temperature self-consistent RMF+BCS calculation of the potential energy surface and single-nucleon wave functions. In the particle-hole channel we employ the relativistic energy functional DD-PC1 [54]. As noted in Sec. II, the parameters of the finite-range separable pairing force were originally

adjusted to reproduce the pairing gap at the Fermi surface in symmetric nuclear matter as calculated with the Gogny D1S force. However, a number of RMF-based studies have shown that in finite nuclei the strength parameters of this force need to be fine tuned, especially for heavy nuclei [57,58]. Here the strengths have been adjusted to reproduce the empirical pairing gaps of ^{226}Th. The assumption is that the fissioning nucleus is in thermal equilibrium at temperature T. The self-consistent RMF+BCS calculation provides a deformation energy surface $F(\boldsymbol{q})$, and variations of the free energy between two points $\boldsymbol{q}_1$ and $\boldsymbol{q}_2$ are given by $\delta F|_T = F(\boldsymbol{q}_1, T) - F(\boldsymbol{q}_2, T)$ [45]. The internal excitation energy $E^*_{\text{int.}}$ of a nucleus at temperature T is defined as the difference between the total binding energy of the equilibrium RMF+BCS minimum at temperature T and at $T = 0$.

In a second step the computer code FELIX (version 2.0) [16] is used for the TDGCM+GOA time evolution. The time step is $\delta t = 5 \times 10^{-4}$ zs. The charge and mass distributions are calculated after 2×10^5 time steps, corresponding to 100 zs. The scission configurations are defined by using the Gaussian neck operator $\hat{Q}_N = \exp[-(z - z_N)^2/a_N^2]$, where $a_N = 1$ fm and z_N is the position of the neck [59]. We define the prescission domain by $\langle \hat{Q}_N \rangle > 2$ and consider the frontier of this domain as the scission contour. Just as in our pervious study of Ref. [42], the parameters of the additional imaginary absorption potential that takes into account the escape of the collective wave packet in the domain outside the region of calculation [16] are: the absorption rate $r = 20 \times 10^{22}\ \text{s}^{-1}$, and the width of the absorption band $w = 1.5$. Following Ref. [18], the fission yields are obtained by convoluting the raw flux with a Gaussian function of the number of particles. The width is set to 4 units for the mass yields, and 1.6 for the charge yields.

A. Temperature-dependent fission barriers and inertia tensors

Figure 1 displays the free energy of ^{226}Th along the least-energy fission pathway for temperatures ranging between zero and 1.25 MeV. The heights of the fission barriers as functions of temperature T are plotted in Fig. 2. At $T = 0$ the mean-field equilibrium state is located at $(\beta_{20}, \beta_{30}) \sim (0.20, 0.15)$. Similar to the results obtained with the functional PC-PK1 [60] in Ref. [42], a triple-humped barrier is predicted along the static fission path with the barrier heights 5.22, 6.32, and 5.16 MeV from the inner to the outer barriers, respectively. One notices that the free energy curves do not change significantly for temperatures $T < 0.75$ MeV, except for a modest increase of the height of the first and second barriers. The barriers start decreasing as temperature increases beyond $T = 0.75$ MeV, and at these higher temperatures the nucleus exhibits a spherical equilibrium shape. We note that although the second (B_{II}) and third (B_{III}) barriers increase slightly when $T \geqslant 1$ MeV, the depths of the second and third potential wells decrease with temperature for all T. At $T = 0.5, 0.75, 1.0$, and 1.25 MeV the corresponding internal excitation energies $E^*_{\text{int.}}$ are: 2.58, 8.71, 16.56, and 27.12 MeV, respectively.

The evolution of the barrier heights as function of temperature, shown in Fig. 2, can be attributed to different rates of damping of pairing correlations and shell effects, as discussed in Ref. [45]. In Fig. 3 we plot the pairing energy for the equilibrium ground state, the fission isomer, the top of the first and second barrier of ^{226}Th. The pairing energies display a rapid decrease with temperature, and completely vanish beyond $T = 0.75$ MeV. This is, of course, also the temperature at which the barrier heights start decreasing.

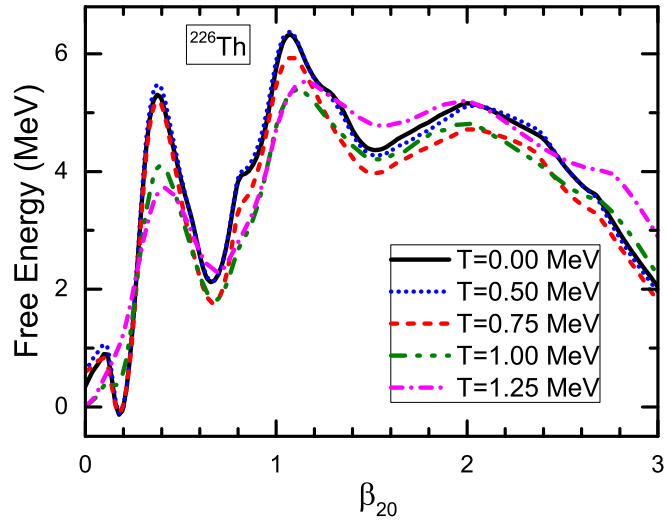

FIG. 1. Free energy (in MeV) along the least-energy fission pathway in ^{226}Th for finite temperatures $T = 0.0, 0.5, 0.75$, 1.0, and 1.25 MeV. All curves are normalized to their values at equilibrium minimum.

The two-dimensional deformation free energy surfaces in the collective space (β_{20}, β_{30}) at $T = 0.0,\ 0.5,\ 0.75,\ 1.0$, and 1.25 MeV are shown in Fig. 4. Only configurations with $\hat{Q}_N \geqslant 2$ are plotted, and the frontier of this domain determines the scission contour. The deformation surfaces at $T = 0.0$ and 0.5 are almost indistinguishable. The ridge separating the asymmetric and symmetric fission valleys gradually decreases with temperature for $T \geqslant 0.75$ MeV. The scission

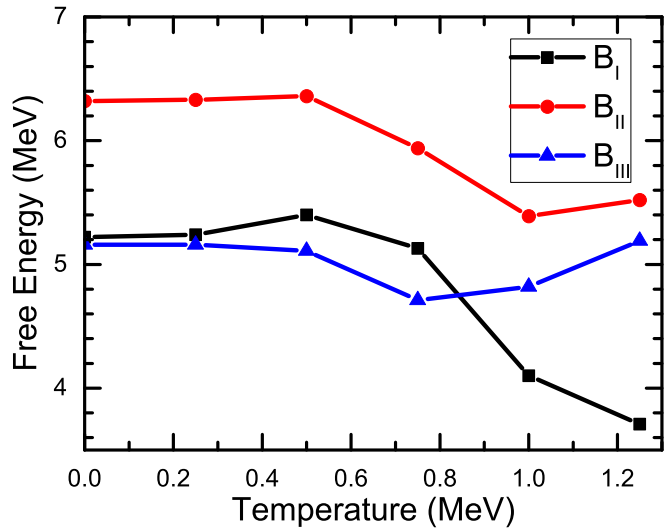

FIG. 2. Evolution of the first (B_{I}), second (B_{II}), and third (B_{III}) barrier heights in the free energy of ^{226}Th, as functions of temperature.

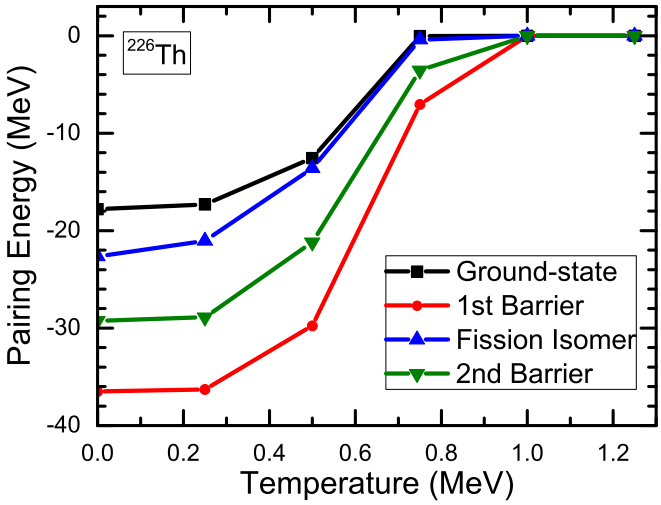

FIG. 3. Temperature dependence of the pairing energy in the RMF+BCS equilibrium minimum, in the fission isomer, and at the top of the first and second barriers in ^{226}Th.

contour at various temperatures displays similar patterns, that is, it starts from an elongated symmetric point at $\beta_{20} \sim 5.5$, and evolves to a minimal elongation $\beta_{20} \sim 3.0$ as asymmetry increases.

For the two-dimensional space of collective deformation coordinates three independent components $\mathcal{M}_{11}$, $\mathcal{M}_{12}$, and

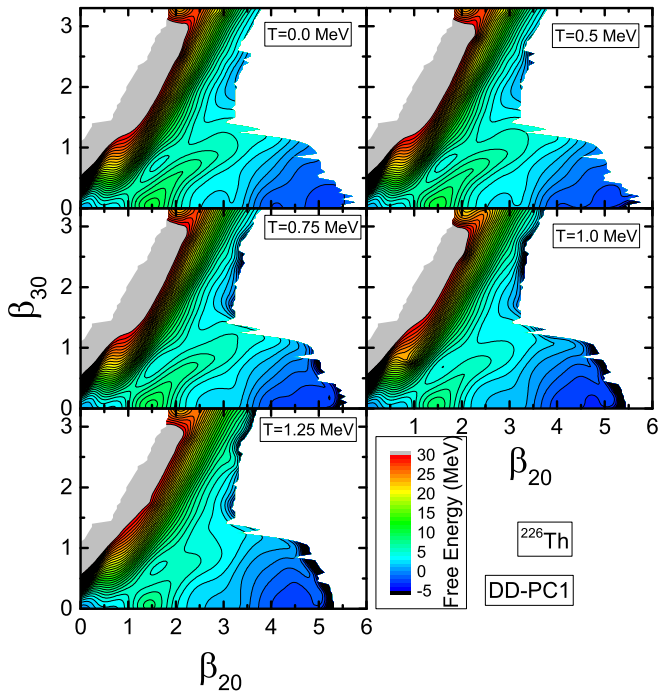

FIG. 4. Free energy F of ^{226}Th in the (β_{20}, β_{30}) plane for finite temperatures $T = 0.0, 0.5, 0.75, 1.0$, and 1.25 MeV. In each panel energies are normalized with respect to the corresponding value at the equilibrium minimum, and contours join points on the surface with the same energy (in MeV). The energy surfaces are calculated with the relativistic density functionals DD-PC1 [54], and the pairing interaction Eq. (12). The contour interval is 1.0 MeV.

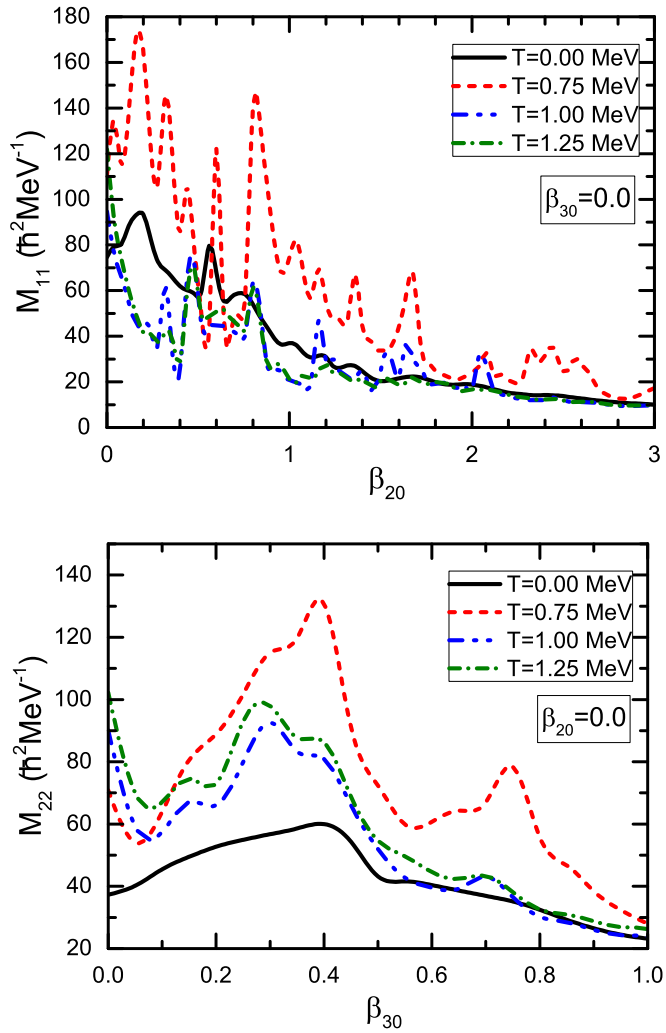

FIG. 5. The $\mathcal{M}_{11}$ component of the mass tensor of ^{226}Th as function of the quadrupole deformation β_{20} (top panel), and the $\mathcal{M}_{22}$ component as function of the octupole deformation β_{30} (bottom panel) for finite temperatures $T = 0.0, 0.75, 1.0$, and 1.25 MeV.

$\mathcal{M}_{22}$ determine the mass tensor. In the present case the indices 1 and 2 refer to the β_{20} and β_{30} degrees of freedom, respectively. In Fig. 5 the evolution of the $\mathcal{M}_{11}$ component of the collective mass with the quadrupole deformation parameter β_{20}, and the $\mathcal{M}_{22}$ component as function of the octupole deformation β_{30}, are shown for different temperatures. One first notices that $\mathcal{M}_{11}$ exhibits more oscillations that reflect the complex underlying structure of level crossings, while $\mathcal{M}_{22}$ displays a smooth behavior as a function of octupole deformation at $T = 0$. In the interval $T = 0 \sim 0.75$ MeV both components generally increase with temperature, due to the weakening of pairing correlations and reduction of pairing gaps for $T > 0$ MeV. Note that in the first approximation the effective collective mass $\mathcal{M} \propto \Delta^{-2}$, where Δ is the pairing gap [61]. After the pairing phase transition has occurred $\mathcal{M}_{11}$ and $\mathcal{M}_{22}$ decrease as a consequence of the weakening of shell effects, except for rather large values at the spherical shape. A similar behavior was also observed in studies based on nonrelativistic Skyrme [44] and Gogny functionals [49].

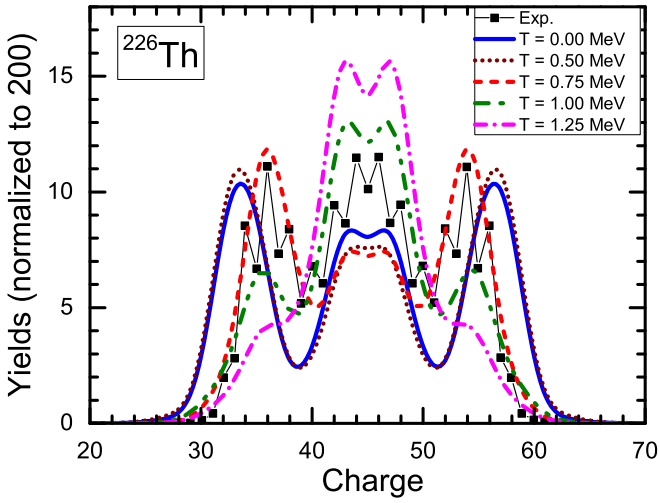

FIG. 6. Charge yields for induced fission of ^{226}Th. The collective potentials and perturbative cranking inertia tensors for the finite temperatures $T = 0.0, 0.5, 0.75, 1.00$, and 1.25 MeV are used in the calculations. The corresponding internal excitation energies are $E^*_{\text{int.}} = 0.0$, 2.58, 8.71, 16.56, and 27.12 MeV, respectively. The average excitation energy of the initial state ($E^*_{\text{coll.}}$) is chosen 1 MeV above the corresponding second fission barrier B_{II}. The experimental charge yields for ^{226}Th(γ, f) are from Ref. [2].

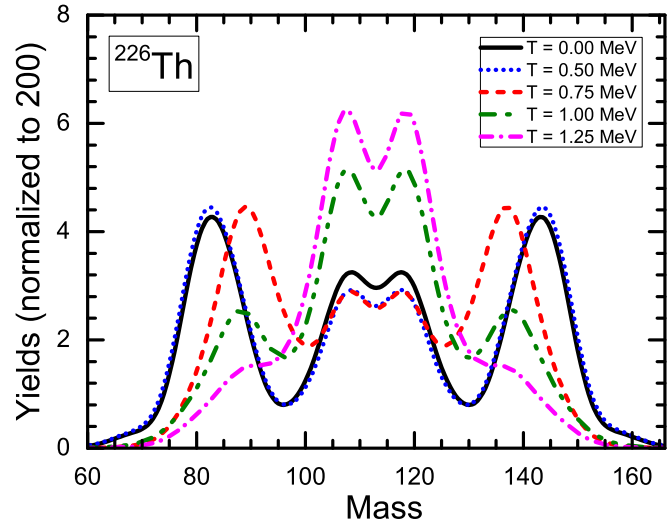

FIG. 7. Same as Fig. 6, but for preneutron emission mass yields.

B. Evolution of charge and mass fragment distributions with temperature

The dynamics of induced fission of ^{226}Th at different temperatures is explored using the time-dependent generator coordinate method (TDGCM) in the Gaussian overlap approximation (GOA). The potential entering the collective Hamiltonian Eq. (17) is given by the Helmholtz free energy $F = E(T) - TS$, with $E(T)$ the RMF+BCS deformation energy in the (β_{20}, β_{30}) plane, and the mass tensor is calculated using Eq. (22). The average energy of the initial state $E^*_{\text{coll.}}$ is chosen 1 MeV above the corresponding second (higher) fission barrier B_{II}.

The preneutron emission charge and mass yields obtained with the TDGCM+GOA, and normalized to $\sum_A Y(A) = 200$, are shown in Figs. 6 and 7, respectively. The experimental fragment charge distribution of ^{226}Th [2] is also included in the plot of Fig. 6. For $T = 0$ MeV the calculation reproduces the trend of the data except, of course, the odd-even staggering. In more detail, however, the predicted asymmetric peaks are located at $Z = 34$ and $Z = 56$, two mass units away from the experimental asymmetric peaks at $Z = 36$ and $Z = 54$. The empirical yield for symmetric fission is somewhat underestimated in the zero-temperature calculation. This picture does not change quantitatively for $T = 0.5$ MeV, as this temperature corresponds to an internal excitation energy of only $E^*_{\text{int.}} = 2.58$ MeV and, therefore, the collective potential and mass tensor are not modified significantly (cf. Sec. III A).

At temperature $T = 0.75$ MeV the asymmetric peaks of the charge yields are predicted at $Z = 36$ and $Z = 54$, in excellent agreement with the empirical values. However, the symmetric fission peak is still lower than the experimental one. The corresponding internal excitation energy of the nucleus is $E^*_{\text{int.}} = 8.71$ MeV. With a further increases of the temperature to $T = 1.0$ MeV, corresponding to $E^*_{\text{int.}} = 16.56$ MeV, the yields of the asymmetric peaks at $Z = 36$ and $Z = 54$ decrease, whereas the symmetric peak increases above the experimental value. This can in part be attributed to the decreases of the ridge separating the asymmetric and symmetric fission valleys, as shown in Fig. 4. It is interesting to note that the experimental charge yield distribution lies between our theoretical results obtained for $E^*_{\text{int.}} = 8.71$ and 16.56 MeV. Indeed, the experimental results were obtained in photoinduced fission with photon energies in the interval 8–14 MeV, with a peak value of $E_\gamma = 11$ MeV [2]. Finally, the calculated charge distribution becomes almost completely symmetric at the highest temperature considered in the present study: $T = 1.25$ MeV, corresponding to an internal excitation energy of $E^*_{\text{int.}} = 27.12$ MeV.

The calculated preneutron emission mass yields for different temperatures are shown in Fig. 7. Analogous to the charge distributions shown in Fig. 6, a three-peak structure is obtained with the asymmetric peaks located at $A = 83$ and $A = 143$, for $T = 0.0$ and 0.5 MeV. At $T = 0.75$ MeV the asymmetric peaks shift by 6 mass units to $A = 89$ and $A = 137$. With a further increases of temperature the yields of the asymmetric peaks decrease, while the symmetric-fission peak is enhanced. The calculated distribution becomes symmetric at $T = 1.25$ MeV.

IV. SUMMARY

We have explored the dynamics of induced fission of ^{226}Th in a theoretical framework based on the finite-temperature time-dependent generator coordinate method (TDGCM) in the Gaussian overlap approximation (GOA). The collective Hamiltonian is determined by the temperature-dependent free energy and perturbative cranking mass tensor in the two-dimensional space of quadrupole and octupole deformations (β_{20}, β_{30}), calculated using the finite-temperature multidimensionally constrained relativistic mean-field plus BCS model. The relativistic energy density functional DD-PC1 has

been employed in the particle-hole channel, and pairing correlations treated in the BCS approximation using a separable pairing force of finite range. The TDGCM+GOA is used to propagate the initial collective state in time and describe fission dynamics.

The critical temperature for the pairing phase transition of ^{226}Th is at $T \approx 0.75$ MeV. At lower temperatures one notices only small changes in the potential (free) energy surface, while the collective mass increases because of the weakening of pairing correlations. The fission barriers start to decrease at $T > 0.75$ MeV, as well as the ridge separating the symmetric and asymmetric fission valleys. The components of the mass tensor decrease after the pairing phase transition.

The preneutron emission charge and mass distributions are calculated using the FELIX code (version 2.0), which is the most recent implementation of the TDGCM+GOA model. Although the empirical triple-humped structure of the fission charge and mass distributions can qualitatively be described without taking into account temperature effects, the experimental positions of the asymmetric peaks and the symmetric-fission yield can only be accurately reproduced in the TDGCM+GOA by using the finite-temperature collective potential and inertia tensor. The model predicts a transition from asymmetric to symmetric fission of ^{226}Th as the internal excitation energy increases. The charge and mass distributions are determined by the collective potential and mass tensor, thus sensitive to the internal excitation energies of the compound nucleus, while the total flux as a function of time is more sensitive to the energy of the collective initial state.

The time-dependent and fully quantum mechanical analysis of induced fission dynamics, reported in this work, has been performed in the two-dimensional (2D) space of quadrupole and octupole deformations. The choice of collective degrees of freedom is empirical but is also determined by available computing resources. In the present case the coupling between the quadrupole (elongation) and octupole (mass asymmetry) degrees of freedom determines the observed charge fragment distribution through the spreading of the collective wave packet. Studies based on semiphenomenological and microscopic methods have indicated that additional collective degrees of freedom could have a pronounced effect on fission dynamics. For instance, hexadecapole deformation, or the coupling between shape and pairing degrees of freedom [40]. However, at present the computational cost of calculations with more than two degrees of freedom is still excessively high. In a recent analysis of Ref. [17] it has been pointed out that, for a regular discretization of the collective space, each additional dimension multiplies both the calculation time of the deformation energy surface and the evolution time of the TDGCM equations by approximately a factor hundred. Even using the spectral finite element discretization of the collective space, in the example of ^{240}Pu the authors estimate that a 3D calculation in the space (q_{20}, q_{30}, q_{40}) would require $\approx 5 \times 10^6$ points in the collective space. Thus, even though the inclusion of additional collective degrees of freedom is certainly important, currently the computational aspect of such an extension is still very challenging. Future studies will certainly consider the effect of additional shape and possibly pairing dynamical variables.

ACKNOWLEDGMENTS

This work has been undertaken as part of the Inter-Governmental S&T Cooperation Project between China and Croatia. It has also been supported in part by the QuantiXLie Centre of Excellence, a project cofinanced by the Croatian Government and European Union through the European Regional Development Fund, the Competitiveness and Cohesion Operational Programme (KK.01.1.1.01). Calculations have been performed in part at the HPC Cluster of KLTP/ITP-CAS and the Supercomputing Center, CNIC of CAS. S.G.Z. was supported by the National Key R&D Program of China (2018YFA0404402), the NSF of China (11525524, 11621131001, 11647601, 11747601, and 11711540016), the CAS Key Research Program of Frontier Sciences (QYZDB-SSWSYS013), the CAS Key Research Program (XDPB09), and the IAEA CRP "F41033".

[1] N. Schunck and L. M. Robledo, Rep. Prog. Phys. **79**, 116301 (2016).
[2] K.-H. Schmidt, S. Steinhauser, C. Bockstiegel, A. Grewe, A. Heinz, A. Junghans, J. Benlliure, H.-G. Clerc, M. de Jong, J. Muller, M. Pfutzner, and B. Voss, Nucl. Phys. A **665**, 221 (2000).
[3] A. N. Andreyev, M. Huyse, and P. Van Duppen, Rev. Mod. Phys. **85**, 1541 (2013).
[4] S. Isaev, R. Prieels, T. Keutgen, J. Van Mol, Y. El Masri, and P. Demetriou, Nucl. Phys. A **809**, 1 (2008).
[5] I. V. Ryzhov, S. G. Yavshits, G. A. Tutin, N. V. Kovalev, A. V. Saulski, N. A. Kudryashev, M. S. Onegin, L. A. Vaishnene, Y. A. Gavrikov, O. T. Grudzevich, V. D. Simutkin, S. Pomp, J. Blomgren, M. Osterlund, P. Andersson, R. Bevilacqua, J. P. Meulders, and R. Prieels, Phys. Rev. C **83**, 054603 (2011).
[6] A. Sen, T. K. Ghosh, S. Bhattacharya, K. Banerjee, C. Bhattacharya, S. Kundu, G. Mukherjee, A. Asgar, A. Dey, A. Dhal, M. M. Shaikh, J. K. Meena, S. Manna, R. Pandey, T. K. Rana, P. Roy, T. Roy, V. Srivastava, and P. Bhattacharya, Phys. Rev. C **96**, 064609 (2017).
[7] R. Leguillon, K. Nishio, K. Hirose, H. Makii, I. Nishinaka, R. Orlandi, K. Tsukada, J. Smallcombe, S. Chiba, Y. Aritomo, T. Ohtsuki, R. Tatsuzawa, N. Takaki, N. Tamura, S. Goto, I. Tsekhanovich, C. Petrache, and A. Andreyev, Phys. Lett. B **761**, 125 (2016).
[8] P. Demetriou and S. Goriely, Nucl. Phys. A **695**, 95 (2001).
[9] K. Hirose, K. Nishio, S. Tanaka, R. Leguillon, H. Makii, I. Nishinaka, R. Orlandi, K. Tsukada, J. Smallcombe, M. J. Vermeulen, S. Chiba, Y. Aritomo, T. Ohtsuki, K. Nakano, S. Araki, Y. Watanabe, R. Tatsuzawa, N. Takaki, N. Tamura, S. Goto, I. Tsekhanovich, and A. N. Andreyev, Phys. Rev. Lett. **119**, 222501 (2017).
[10] V. Simutkin, S. Pomp, J. Blomgren, M. Österlund, R. Bevilacqua, P. Andersson, I. Ryzhov, G. Tutin, S. Yavshits, L.

Vaishnene, M. Onegin, J. Meulders, and R. Prieels, Nucl. Data Sheets **119**, 331 (2014).
[11] D. Ramos, M. Caamaño, F. Farget, C. Rodríguez-Tajes, L. Audouin, J. Benlliure, E. Casarejos, E. Clement, D. Cortina, O. Delaune, X. Derkx, A. Dijon, D. Doré, B. Fernández-Domínguez, G. de France, A. Heinz, B. Jacquot, A. Navin, C. Paradela, M. Rejmund, T. Roger, M.-D. Salsac, and C. Schmitt, Phys. Rev. C **97**, 054612 (2018).
[12] H. Naik, G. N. Kim, and K. Kim, Phys. Rev. C **97**, 014614 (2018).
[13] J. Berger, M. Girod, and D. Gogny, Comput. Phys. Commun. **63**, 365 (1991).
[14] H. Goutte, J. F. Berger, P. Casoli, and D. Gogny, Phys. Rev. C **71**, 024316 (2005).
[15] W. Younes and D. Gogny, Fragment Yields Calculated in a Time-Dependent Microscopic Theory of Fission, Technical Report Lawrence Livermore National Laboratory, 2012 .
[16] D. Regnier, N. Dubray, M. Verriere, and N. Schunck, Comput. Phys. Commun. **225**, 180 (2018).
[17] D. Regnier, N. Dubray, N. Schunck, and M. Verriere, EPJ Web Conf. **146**, 04043 (2017).
[18] D. Regnier, N. Dubray, N. Schunck, and M. Verriere, Phys. Rev. C **93**, 054611 (2016).
[19] D. Regnier, M. Verriere, N. Dubray, and N. Schunck, Comput. Phys. Commun. **200**, 350 (2016).
[20] A. Zdeb, A. Dobrowolski, and M. Warda, Phys. Rev. C **95**, 054608 (2017).
[21] M. Verriere, N. Dubray, N. Schunck, D. Regnier, and P. Dossantos-Uzarralde, EPJ Web Conf. **146**, 04034 (2017).
[22] D. Vretenar, A. Afanasjev, G. Lalazissis, and P. Ring, Phys. Rep. **409**, 101 (2005).
[23] J. Meng, H. Toki, S. G. Zhou, S. Q. Zhang, W. H. Long, and L. S. Geng, Prog. Part. Nucl. Phys. **57**, 470 (2006).
[24] *Relativistic Density Functional for Nuclear Structure*, edited by J. Meng, International Review of Nuclear Physics, Vol. 10 (World Scientific, Singapore 2016).
[25] S.-G. Zhou, Phys. Scr. **91**, 063008 (2016).
[26] T. Burvenich, M. Bender, J. A. Maruhn, and P.-G. Reinhard, Phys. Rev. C **69**, 014307 (2004).
[27] V. Blum, J. Maruhn, P.-G. Reinhard, and W. Greiner, Phys. Lett. B **323**, 262 (1994).
[28] W. Zhang, S.-S. Zhang, S.-Q. Zhang, and J. Meng, Chin. Phys. Lett. **20**, 1694 (2003).
[29] M. Bender, P.-H. Heenen, and P.-G. Reinhard, Rev. Mod. Phys. **75**, 121 (2003).
[30] H.-F. Lu, L.-S. Geng, and J. Meng, Chin. Phys. Lett. **23**, 2940 (2006).
[31] Z. P. Li, T. Nikšić, D. Vretenar, P. Ring, and J. Meng, Phys. Rev. C **81**, 064321 (2010).
[32] H. Abusara, A. V. Afanasjev, and P. Ring, Phys. Rev. C **82**, 044303 (2010).
[33] H. Abusara, A. V. Afanasjev, and P. Ring, Phys. Rev. C **85**, 024314 (2012).
[34] B.-N. Lu, E.-G. Zhao, and S.-G. Zhou, Phys. Rev. C **85**, 011301(R) (2012).
[35] B.-N. Lu, J. Zhao, E.-G. Zhao, and S.-G. Zhou, Phys. Rev. C **89**, 014323 (2014).
[36] J. Zhao, B.-N. Lu, D. Vretenar, E.-G. Zhao, and S.-G. Zhou, Phys. Rev. C **91**, 014321 (2015).
[37] S. E. Agbemava, A. V. Afanasjev, D. Ray, and P. Ring, Phys. Rev. C **95**, 054324 (2017).
[38] V. Prassa, T. Nikšić, G. A. Lalazissis, and D. Vretenar, Phys. Rev. C **86**, 024317 (2012).
[39] J. Zhao, B.-N. Lu, T. Niksic, and D. Vretenar, Phys. Rev. C **92**, 064315 (2015).
[40] J. Zhao, B.-N. Lu, T. Niksic, D. Vretenar, and S.-G. Zhou, Phys. Rev. C **93**, 044315 (2016).
[41] J. Zhao, B.-N. Lu, E.-G. Zhao, and S.-G. Zhou, Phys. Rev. C **95**, 014320 (2017).
[42] H. Tao, J. Zhao, Z. P. Li, T. Niksic, and D. Vretenar, Phys. Rev. C **96**, 024319 (2017).
[43] A. L. Goodman, Nucl. Phys. A **352**, 30 (1981).
[44] Y. Zhu and J. C. Pei, Phys. Rev. C **94**, 024329 (2016).
[45] N. Schunck, D. Duke, and H. Carr, Phys. Rev. C **91**, 034327 (2015).
[46] J. D. McDonnell, W. Nazarewicz, and J. A. Sheikh, Phys. Rev. C **87**, 054327 (2013).
[47] J. D. McDonnell, W. Nazarewicz, J. A. Sheikh, A. Staszczak, and M. Warda, Phys. Rev. C **90**, 021302(R) (2014).
[48] J. C. Pei, W. Nazarewicz, J. A. Sheikh, and A. K. Kerman, Phys. Rev. Lett. **102**, 192501 (2009).
[49] V. Martin and L. M. Robledo, Int. J. Mod. Phys. E **18**, 861 (2009).
[50] F. A. Ivanyuk, C. Ishizuka, M. D. Usang, and S. Chiba, Phys. Rev. C **97**, 054331 (2018).
[51] J. Randrup and P. Möller, Phys. Rev. C **88**, 064606 (2013).
[52] H. Pasca, A. V. Andreev, G. G. Adamian, and N. V. Antonenko, Phys. Lett. B **760**, 800 (2016).
[53] J. L. Egido, P. Ring, and H. J. Mang, Nucl. Phys. A **451**, 77 (1986).
[54] T. Nikšić, D. Vretenar, and P. Ring, Phys. Rev. C **78**, 034318 (2008).
[55] Y. Tian, Z. Y. Ma, and P. Ring, Phys. Lett. B **676**, 44 (2009).
[56] Y. Gambhir, P. Ring, and A. Thimet, Ann. Phys. (NY) **198**, 132 (1990).
[57] L. J. Wang, B. Y. Sun, J. M. Dong, and W. H. Long, Phys. Rev. C **87**, 054331 (2013).
[58] A. V. Afanasjev and O. Abdurazakov, Phys. Rev. C **88**, 014320 (2013).
[59] W. Younes and D. Gogny, Phys. Rev. C **80**, 054313 (2009).
[60] P. W. Zhao, Z. P. Li, J. M. Yao, and J. Meng, Phys. Rev. C **82**, 054319 (2010).
[61] L. Moretto and R. Babinet, Phys. Lett. B **49**, 147 (1974).